Construction and applications of an atomic magnetic gradiometer based on nonlinear magneto-optical rotation

Shoujun Xu
*Materials Sciences Division, Lawrence Berkeley National Laboratory, Berkeley, California 94720
and Department of Chemistry, University of California, Berkeley, California 94720*

Simon M. Rochester
Department of Physics, University of California, Berkeley, California 94720-7300

Valeriy V. Yashchuk
Advanced Light Source, Lawrence Berkeley National Laboratory, Berkeley, California 94720

Marcus H. Donaldson
*Materials Sciences Division, Lawrence Berkeley National Laboratory, Berkeley, California 94720
and Department of Chemistry, University of California, Berkeley, California 94720*

Dmitry Budker
*Department of Physics, University of California, Berkeley, California 94720-7300
and Nuclear Sciences Division, Lawrence Berkeley National Laboratory, Berkeley, California 94720*

We report on the design, characterization, and applications of a sensitive atomic magnetic gradiometer. The device is based on nonlinear magneto-optical rotation in alkali-metal (^{87}Rb) vapor and uses frequency-modulated laser light. The magnetic field produced by a sample is detected by measuring the frequency of a resonance in optical rotation that arises when the modulation frequency equals twice the Larmor precession frequency of the Rb atoms. The gradiometer consists of two atomic magnetometers. The rotation of light polarization in each magnetometer is detected with a balanced polarimeter. The sensitivity of the gradiometer is 0.8 nG/Hz$^{1/2}$ for near-dc (0.1 Hz) magnetic fields, with a base line of 2.5 cm. For applications in nuclear magnetic resonance (NMR) and magnetic resonance imaging (MRI), a long solenoid that pierces the magnetic shields provides an ~0.5 G leading field for the nuclear spins in the sample. Our apparatus is particularly suited for remote detection of NMR and MRI. We demonstrate a point-by-point free induction decay measurement and a spin echo reconstructed with a pulse sequence similar to the Carr-Purcell-Meiboom-Gill pulse. Additional applications and future improvements are also discussed. © *2006 American Institute of Physics.* [DOI: 10.1063/1.2336087]

I. INTRODUCTION

Atomic magnetometry as applied to the detection of nuclear magnetism has a rather long history, starting with the pioneering work by Cohen-Tannoudji *et al.* in the 1960s.[1] In that work, alkali vapor was used to measure the magnetization of optically hyperpolarized ^{3}He. Since then, it has been developed by Newbury *et al.*[2] toward a more sensitive and convenient technique. The sensitivity of an optimized, shot-noise limited atomic magnetometer is determined by

$$\delta B \approx 1/(\gamma\sqrt{Nt\tau}), \tag{1}$$

where γ is the atomic gyromagnetic ratio, N is the total number of the gaseous alkali atoms participated in the measurement, t is the measurement time, and τ is the coherence lifetime.

Recently, several novel approaches to atomic magnetometry have been demonstrated with extraordinarily high sensitivities. One approach is the use of potassium vapor at high enough densities that the effect of spin-exchange relaxation effectively cancels.[3,4] This so-called spin-exchange relaxation-free (SERF) technique has achieved a sensitivity of 5 pG/Hz$^{1/2}$. Another path uses low-density rubidium vapor in paraffin-coated cells to reduce the spin-relaxation rate and create ultranarrow resonances in nonlinear magneto-optical rotation.[5,6] The latter technique employs frequency- or amplitude-modulated laser light to synchronously pump alignment in the atomic ground state.[7–9] A narrow resonance occurs when the modulation frequency is equal to twice the Larmor precession frequency γB, allowing precise determination of the magnetic field. With this technique, sensitivity below 10 pG/Hz$^{1/2}$ should also be achievable.

The main objective for the present work is to apply atomic magnetometry to nuclear magnetic resonance (NMR) and magnetic resonance imaging (MRI). NMR and MRI are prominent and versatile techniques that have found applications in many areas.[10,11] However, magnetic resonance techniques suffer from poor sensitivity in low magnetic fields: with conventional Faraday-induction detection using a radio frequency (rf) coil the signal is proportional to the strength of the magnetic field (assuming a given degree of nuclear polarization). Thus alternative detection methods are desirable when the use of high magnetic field is to be avoided.
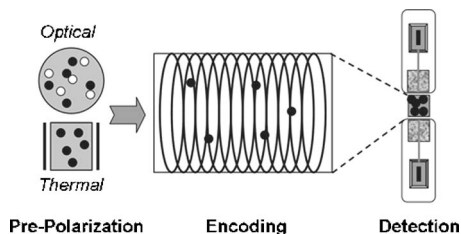
FIG. 1. Concept of remote detection of NMR and MRI with atomic magnetometers. A gradiometer formed by two magnetometers is shown as an example.

Atomic magnetometers[12,13] and superconducting quantum interference devices[14–16] (SQUIDs) have both been proven to possess such sensitivity. Early applications of atomic magnetometers in NMR include measurements of the T_1 relaxation of hyperpolarized xenon[12] and the free induction decay of protons in an ultraweak magnetic field inside a magnetometer.[13] One advantage of atomic magnetometers is that, unlike SQUIDs or superconducting magnets, they do not require cryogenics, making them more convenient and less expensive.

To improve the "filling factor," the degree to which the sample couples to the detector, atomic magnetometry can be combined with a complementary detection scheme—remote detection.[17–19] In remote detection, the spectroscopic (for NMR) and spatial (for MRI) information is stored as time-dependent total magnetization of the sample along the longitudinal axis. Detection is performed at a different location from the encoding region. The encoded information can be recovered via Fourier transformation of the sample magnetization measurement. If the sample is spread out spatially, which precludes efficient NMR detection, the remote detection method can offer a significant advantage, as the sample can be concentrated in the detection region, improving the sensor coupling to the sample (commonly referred to as the filling factor in NMR) and detection efficiency. It also opens up the possibility of implementing more sensitive detection methods for NMR and MRI, including atomic magnetometry. Since the detection is physically separated from the encoding step, the rf magnetic fields and gradient magnetic fields used for spin encoding do not interfere with the sensitive magnetometers.

One additional consideration for low-field NMR and MRI is that thermal magnetization is intrinsically low (typically 10^{-8}). This problem can be circumvented by using prepolarization, for example, through spin exchange with optically pumped rubidium atoms in the case of ^{129}Xe and ^{3}He nuclei[20] (up to tens of percent polarization), or magnetization by a strong magnetic field prior to the encoding step.[21]

Figure 1 illustrates the technique of applying atomic magnetometry to remote detection in low-field NMR and MRI. It contains three essential steps: prepolarization of the nuclear spins, low-field encoding, in which the pulse sequences are applied, and detection with sensitive atomic magnetometers.

Here we describe a new atomic magnetometer which was recently used for remote detection of time-resolved MRI.[21] Compared to the magnetometer used in Ref. 12, the new instrument possesses an improved filling factor, better stability, and an optimal geometry for various applications. The details of our apparatus and characterization are provided in the following sections, followed by examples of NMR measurements and a brief discussion and outlook.

II. APPARATUS

A schematic of the setup is shown in Fig. 2. The main components include a multilayer magnetic shield with internal coils, a pair of rubidium vapor cells, a diode laser with associated control electronics and optics, a piercing solenoid, and electronics for signal amplification and data acquisition.

A. Magnetic shield and internal coils

To reduce the laboratory magnetic field, a five-layer magnetic shield is employed (Fig. 3). The shield is made of a high-permeability alloy (0.1 cm thick). After manufacture (by Amuneal, Inc. according to our design), the shields were annealed in a hydrogen atmosphere. We avoid mechanical stress on the shield and exposure to high magnetic fields after annealing; demagnetization of the shield is not neces-
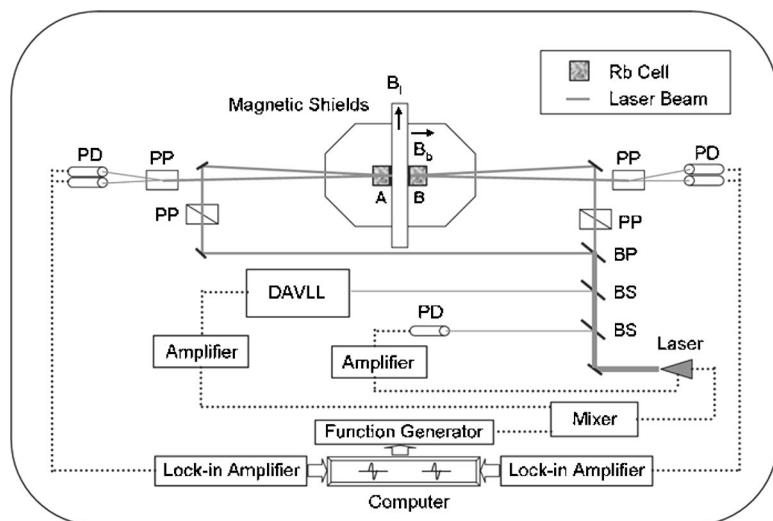

FIG. 2. Schematic of the apparatus. Abbreviations: BS, beam sampler; BP, beam splitter; PD, photodiodes; PP, polarizing prism. The rubidium vapor cells are labeled as A and B. The thickness of the laser beam (gray lines in the diagram) symbolically indicates the relative beam power. In between the two cells is the piercing solenoid. B_l, leading field provided by the piercing solenoid; B_b, bias magnetic field.
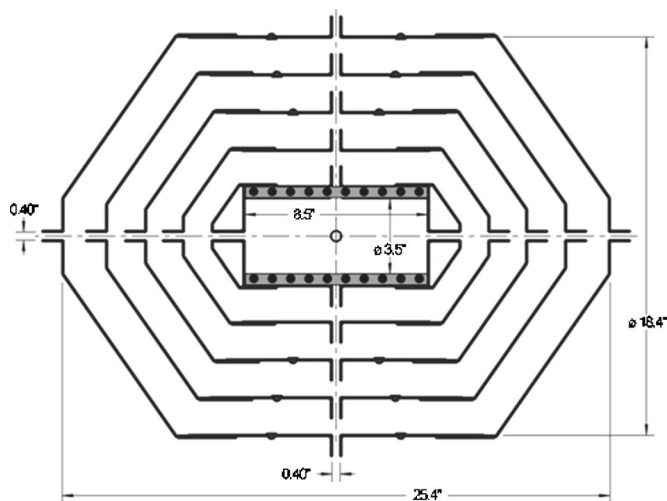
FIG. 3. Cross section of the magnetic shields. Internal coils are indicated with black dots. The Teflon coil holder inside the magnetic shield is shown in gray. The rubidium vapor cells are mounted on a platform located at the center of the magnetic shield (not shown).

sary. Each of the five layers consists of a cylindrical center piece and two removable end caps. The overall shape of each layer approximates a sphere to maximize the shielding factor, while avoiding elements with difficult-to-manufacture shapes. Between the layers, Styrofoam (polymerized in place) is used to hold the shield in place and to provide thermal insulation from the environment. Four ports are available on the cylindrical part and one each on the end caps for each layer. They are aligned, respectively, among different layers during assembly and are used for optical access, the piercing solenoid and sample inlet, cell mounting, and electric connections. The shielding factor of the whole assembly was measured to be better than 10^7 for low-frequency magnetic fields.

A set of coils is mounted on a hollow cylindrical Teflon holder inside the magnetic shield, including a solenoidal bias-field coil, two planar transverse-field coils, and three gradient coils. These coils are used to balance the residual magnetic field and gradients and to provide a bias field. The bias field is directed along the center-to-center line of the rubidium cells, defined as the z axis, and parallel to the laser path (Faraday geometry in optical rotation). Since the sample magnetic field is much smaller than the bias field, the gradiometer is only sensitive to the magnetic field change along the z axis. The z-gradient coil, driven by an adjustable dc source (Krohn-Hite, Model 523), is used to balance the two magnetometers, so that their resonance frequencies are close to each other, usually within 0.5 Hz. The other coils are powered by dry batteries through resistors with low temperature coefficients ($\sim$0.6 ppm/$^\circ$C).

B. Rubidium vapor cells

The vapor cells containing isotopically enriched rubidium-87 (^{87}Rb) used in this apparatus are glass cubes with external dimensions of 1 cm on a side and wall thickness of approximately 1 mm. Compared to a 10 cm diameter cell such as that used in Ref. 12, these cells can be placed much closer to the sample, significantly improving the filling

factor. The inner walls of the cells are coated with a layer of paraffin to minimize relaxation of ground-state polarization due to collisions with the wall.[22] Magnetometers using such buffer-gas-free antireflection coated vapor cells measure the average of the magnetic field over the cell's volume. For a spherical cell, the average field is equal to the field at the center of the cell. While this is not exactly true for the cubic cells used in this work, this is still a reasonable approximation.

The total number of rubidium atoms in the vapor in smaller cells can be increased by raising the operating temperature. The heating method has to be carefully chosen to avoid introducing extra noise. We use twisted Teflon-coated stainless steel wire wound around the outside of the innermost layer of the magnetic shield. The magnetic noise generated by the heating current is largely canceled and shielded by this method. Continuous heating by a current-regulated dc power supply has proven to be the best option.

The paraffin coating melts at approximately 60 $^\circ$C, which sets an upper limit for the cell temperature. The temperature is also constrained by the need to keep the alkali vapor density low enough that the alkali-alkali collisions do not unduly increase the relaxation rate. An operating temperature of 43 $^\circ$C gives maximum signal-to-noise ratio in this apparatus.

The cells are mounted on a Teflon platform. The positions of the cells can be independently adjusted by six nylon alignment screws. A sturdy plastic rod goes through the magnetic shield via the bottom port to connect the platform to a translation stage on the laser table. This allows slight adjustment of the position of the platform from outside of the magnetic shield.

C. Laser control and optical layout

A single laser (New Focus, Vortex 6000), frequency-modulated by driving a piezoelectric transducer in the laser cavity with a function generator, is used for both magnetometers. The beam is first attenuated by neutral-density filters (not shown in Fig. 2). Two 5% beam samplers are used for controlling the laser. The first one feeds a photodiode for power monitoring. The voltage output of the photodiode is amplified and fed back to the laser for constant-power operation. The second one is used for a dichroic atomic vapor laser lock (DAVLL) (the design is described in Ref. 23), employed to lock the laser at the optimal wavelength. It contains an uncoated rubidium cell placed in an $\sim$200 G magnetic field, a quarter-wave plate, and two polarization prisms.[24] Linear magneto-optical rotation is detected by two photodiodes and amplified by a lock-in amplifier (Stanford Research SR530). The output of the appropriately phased lock-in amplifier is fed back to the piezoelectric element of the laser to adjust the wavelength of the laser accordingly. Operation of a DAVLL with frequency-modulated light extends the use of the device that is normally employed with unmodulated light.[23,24]

The main laser beam passes through a 50-50 beam splitter to produce a beam for each magnetometer. For each magnetometer, a polarization prism defines the initial polarization of the incident beam. The diameter of the laser beams at the cells is approximately 2 mm. After passing through a
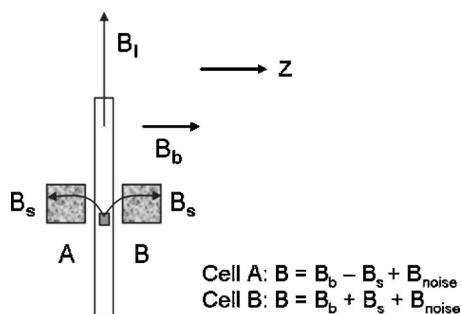
FIG. 4. Illustration of the measurement geometry. B_l, leading field; B_b, bias field; B_{noise}, magnetic noise; B_s, magnetic field generated by the sample. Since the two rubidium cells experience magnetic field of opposite signs due to the sample, the difference between the two measurements will double the signal from the sample, while canceling common-mode noise.

cell, the beam is reflected by an end mirror (aluminum coated on 1 mm glass substrate) mounted close to the back of the cell, passes through the cell again, and then through an analyzing prism oriented at 45° to the initial prism. This balanced polarimeter is sensitive to magneto-optical rotation induced by the Rb vapor.[25]

This double-pass arrangement, in which the beams are reflected back through the cells, was chosen in order to allow the cells to be placed in an optimal position relative to the sample. The resulting increase in optical path length (the rotation is additive on the two passes) is also significant because of the small size of the cells used in this work and reduces the heating requirements for the cells.

D. Piercing solenoid, bias magnetic field, and sample polarization

For NMR applications, a leading field is required for the nuclear spins in the sample. This is provided by a long hollow solenoid that pierces the magnetic shield. The field strength inside the solenoid is ~0.5 G, approximately the earth-field strength. Since the rubidium vapor cells are located far from the ends (which are outside the magnetic shield), the solenoid field is very small at the cell positions.

A bias magnetic field, with a magnitude much larger than the sample magnetic field, is generated to define the detection axis of the gradiometer. This dictates that the sample (which would normally be approximated as a magnetic dipole aligned with the leading field in the piercing solenoid) be offset in the direction of the leading field from the axis connecting the centers of the sensor cells. In practice, the optimal position was chosen by using a calibration solenoid in place of the sample that could be moved along the piercing solenoid. The sample in the detection region produces magnetic fields with opposite directions in the two cells (Fig. 4). Thus, the signal due to magnetization of the sample along the leading field adds in the gradiometer measurements, while common-mode noise (B_{noise}) cancels.

E. Signal detection

The electronics for signal manipulation are fairly simple. For each magnetometer, the differential photocurrent between the photodiode pair is detected by a lock-in amplifier
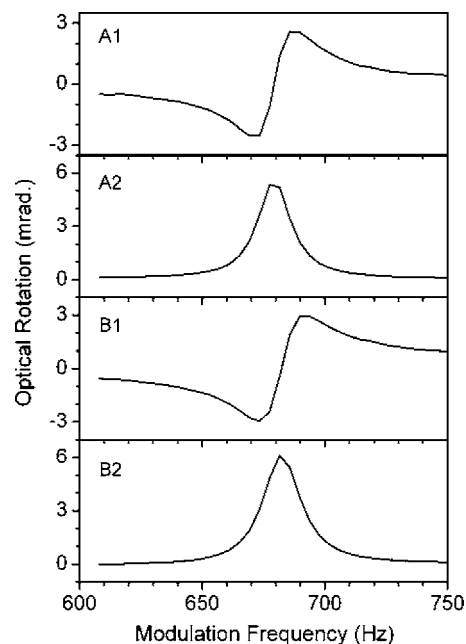

FIG. 5. Synchronous nonlinear magneto-optical rotation as a function of the laser modulation frequency. A1 and A2 are the in-phase and out-of-phase outputs from magnetometer A, respectively. B1 and B2 are the respective in-phase and out-of-phase outputs from magnetometer B. Laser power is ~8 μW for each magnetometer and the detuning is 200 MHz towards lower frequencies from the $F=2 \rightarrow F'=1$ component of the ^{87}Rb D1 line.

(Stanford Research, SR830). The outputs of the lock-in amplifiers are read to a personal computer over a general purpose interface bus (GPIB) connection. A LABVIEW program analyzes the signals, and controls the output frequency of a function generator (Stanford Research DS 345) modulating the laser, using a feedback algorithm described below.

III. CHARACTERIZATION

A. Nonlinear magneto-optical resonance

As part of the initialization of the magnetometer, the laser is detuned ~200 MHz towards lower frequency from the $F=2 \rightarrow F'=1$ component of the ^{87}Rb D1 line in order to produce the maximum optical rotation.[7] With the laser detuning fixed at the optimal position, we sweep the modulation frequency of the laser to observe the nonlinear magneto-optical resonance, which occurs when the modulation frequency is equal to twice the Larmor precession frequency. The presence of a 0.48 mG bias field gives a resonance frequency of ~680 Hz in the absence of the sample. Figure 5 exhibits both the in-phase and out-of-phase (quadrature) outputs from the lock-in amplifier of each magnetometer. The widths of these resonances in the modulation-frequency domain correspond to twice the Rb ground-state coherence-relaxation rate (12 and 13 Hz for the two magnetometers from the scans in Fig. 5). As indicated above [Eq. (1)], the longer the coherence lifetime, the better the sensitivity. To obtain the intrinsic linewidth, we plot the linewidth (equal to that observed in the modulation-frequency domain divided by 2) versus laser power and extrapolate to zero power (Fig. 6). From linear extrapolation, the intrinsic relaxation rate is around 5.4 Hz for both cells, compared to 1.3 Hz for the
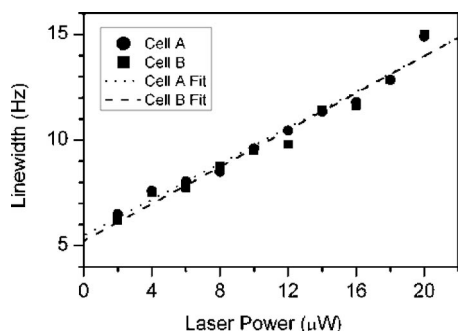
FIG. 6. Resonance linewidth vs laser power. Laser power is measured right before the light beam enters a rubidium cell. The *y* intercepts represent the intrinsic linewidths.

10 cm diameter cell used in Ref. 12. This difference is primarily due to the smaller size of the cells used here, as the mean free path between wall collisions is much shorter. However, because of a factor of ~1000 improvement in the filling factor in the current setup, we gain substantially in overall sensitivity.

B. Data acquisition algorithm

We have explored two strategies for locking a magnetometer to a resonance. The first strategy consists in tracking the resonance frequency by determining the center of the peak in the quadrature signal. This has an advantage of reduced sensitivity to background signals; however, it is slow because at least three points are needed to fit for the center frequency, and the system must be allowed to stabilize each time the modulation frequency is changed. In the second strategy (used for the experiments described below), the in-phase signal from one magnetometer, which is proportional to deviations from resonance in a limited range centered at resonance, is measured, inverted, and fed back to the function generator which modifies the modulation frequency accordingly. The computer-implemented feedback is a proportional and integral (PI) loop, controlled by three parameters: P, I, and an integration range. The feedback signal f and error signal ε are related by

$$f = P\left(\varepsilon + I \int_{-t}^{0} \varepsilon \, dt'\right). \qquad (2)$$

Applying a square wave magnetic field as a test signal (such as the ones shown in Figs. 7 and 8), we set appropriate values for P and I according to the following algorithm. With I set to zero, increase P until the system begins to oscillate. Then set P at ~50% of the oscillation threshold and with a fixed integration range, typically set as 5 s, adjust I to optimize the response of the apparatus to minimum distortion from the testing square wave.

The magnetometer controlled by the feedback loop, designated as the primary channel, is thus always on resonance. The in-phase signal from the other magnetometer, the passive channel, is the differential measurement, free of common-mode noise. The feedback loop maintains the modulation frequency in the most sensitive regime, since the slope of the resonance feature is maximal at the center of resonance, which is 0.6 mrad/Hz. The advantages of a soft-
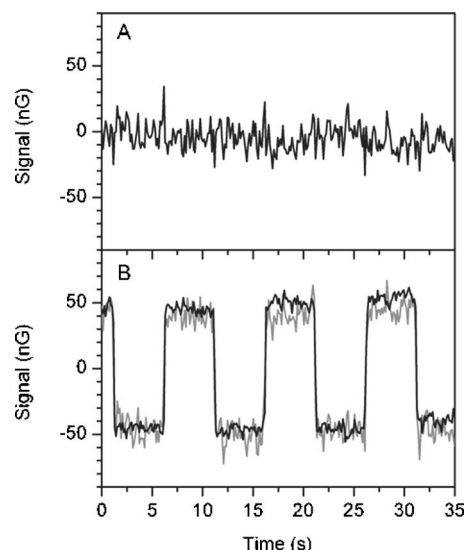

FIG. 7. Demonstration of the cancellation of a common-mode magnetic field by the gradiometer. A uniform 100 nG (peak-to-peak) square-wave magnetic field is applied using the *z* coil. Plot A shows the differential gradiometer signal. Plot B shows the signal from each arm of the magnetometer.

ware PI loop include insensitivity to noise and flexibility in adjusting the parameters of the response function.

C. Noise and sensitivity

A range of sources can contribute to the noise, including ambient air flow, stray light, dark current of the photodiodes, electronic noise from the lock-in amplifiers, and the mechanical vibrations of various components. One particularly significant noise comes from air circulation in the environment, causing refractive index fluctuation of the air in the laser path that leads to random optical rotation. This effect is greatly reduced by enclosing the entire beam path. The stray light is also blocked. The photodiodes are connected in pairs without bias voltage so that only the differential photocurrent is amplified, further reducing the dark current.

To demonstrate the common-mode cancellation of the gradiometer, a common-mode magnetic field modulated at 0.1 Hz is generated by the *z* coil. As shown in Fig. 7, both magnetometers experience the magnetic field, while no evident signal is observed in the gradiometer. The common-mode-rejection ratio is estimated to be no worse than 20.

For calibration, a small gradient field square wave with frequency of 0.1 Hz is generated by the *z*-gradient coil. The measurements are presented in Fig. 8. Plot A shows a recording of the gradiometer signal with closed feedback loop on the primary-channel magnetometer. Plot B shows the signal from the primary-channel magnetometer with feedback loop open. By taking the differential signal between the two magnetometers, as mentioned above, the common-mode drift is reduced. In addition, the signal-to-noise ratio (SNR), limited by the intrinsic noise of the individual sensors, is improved by a factor of $\sqrt{2}$. The time constant for the measurement is 30 ms. The sensitivity of the gradiometer is estimated to be 0.8 nG/Hz$^{1/2}$ for the geometry applied in this work. The polarization noise level is therefore ~10^{-3} mrad/Hz$^{1/2}$.
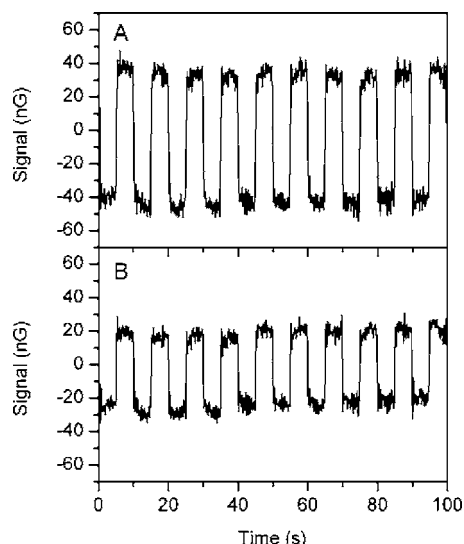
FIG. 8. Sensitivity comparison between the gradiometer and the primary channel. The test signal is a 40 nG magnetic field modulated at 0.1 Hz, produced by the z-gradient coil which is powered by a function generator. Plot A shows the gradiometer signal with closed feedback loop on the primary-channel magnetometer. Plot B shows the signal from the primary-channel magnetometer with the feedback loop open.

IV. APPLICATIONS

We have reported the application of this apparatus in MRI.[21] Here we show the remote detection of NMR. The setup, which is similar to the one used in Ref. 21, is schematically exhibited in Fig. 9. Water flows continuously through three consecutive regions. It is first prepolarized by a permanent magnet with field strength of 3 kG. It then flows into a plastic sample holder located at the center of the encoding field of 31 G, corresponding to 131.3 kHz resonance frequency for protons. A rf coil tuned to the resonance frequency is used to excite the sample nuclei. Pulse sequences are controlled with a TecMag console (Orion 1999). Finally, encoded water flows into the gradiometer and returns through the same port for drain, producing magnetic fields with opposite directions in the two cells for detection. The base line of the measurement is set at the signal correspond-
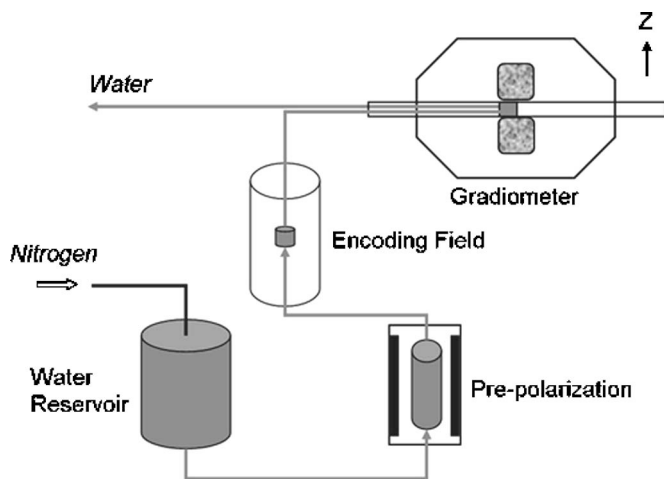

FIG. 9. The sample-flow diagram for NMR experiment. Objects containing water are shown in gray.
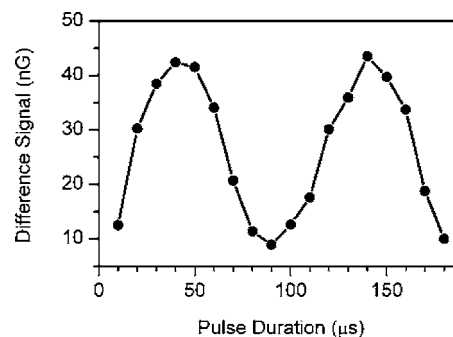

FIG. 10. Determining the time duration of the $\pi/2$ pulse. A pulse train with incremented pulse durations is applied in the encoding region. The difference signal measured by the gradiometer is plotted vs the pulse duration.

ing to the initial magnetization M_z of the sample when no rf pulses are applied. The largest signal change (drop) is referred to as the maximum signal. The flow rate is set to be as fast as 30 ml/min to minimize the relaxation of the nuclear polarization during the travel from the prepolarization region to the detection region.

For NMR measurements, the $\pi/2$ pulse duration is determined by varying the pulse length and recording the corresponding magnetization of the sample (Fig. 10). The first maximum corresponds to a π pulse as the magnetization is totally inverted so the gradiometer detects the largest difference. The minima correspond to $2n\pi$ pulses, $n=0,1,2$, since the magnetization is simply tipped back to its original direction. According to the data exhibited in Fig. 10, a $\pi/2$ pulse should be of 22 μs duration.

Free induction decay (FID) of the protons can be detected remotely by using two $\pi/2$ pulses with a variable delay between them. The frequency of the pulses is tuned to 132.7 kHz in order to shift the central FID frequency away from zero. The first $\pi/2$ pulse rotates the magnetization of the sample into the transverse plane (xy). During the delay, the magnetization precesses in the 31 G field. Then it is tipped back into the longitudinal direction z by another $\pi/2$ pulse. The stored magnetization is read out by the gradiometer. The magnetization as a function of the delay time, averaged over ten data sets, is shown in Fig. 11. The Fourier transform of the FID gives the spectrum in the frequency domain. The peak frequency of 1.4 kHz is the difference between the carrier frequency and the resonance frequency. The full width at half maximum is approximately 400 Hz.

A more complicated pulse sequence (shown in Fig. 12, panel A), similar to a Carr-Purcell-Meiboom-Gill (CPMG) pulse,[10] was also applied to obtain spin echo. A normal CPMG pulse is composed of an excitation $\pi/2$ pulse followed by a train of π pulses which have a 90° phase shift relative to the $\pi/2$ pulse. The temporal spacing (echo time) between consecutive π pulses is twice the time between the first $\pi/2$ pulse and the first π pulse. Thus the coherence lost during precession due to field inhomogeneity can be recovered by inverting the magnetization each time by a π_y pulse. Multiple (n) π pulses can be repeated until the total time of the pulse sequence reaches the intrinsic transverse relaxation time. (We have tried as many as 300 π pulses, corresponding to a total time of 600 ms.) Because we detect the spin echo
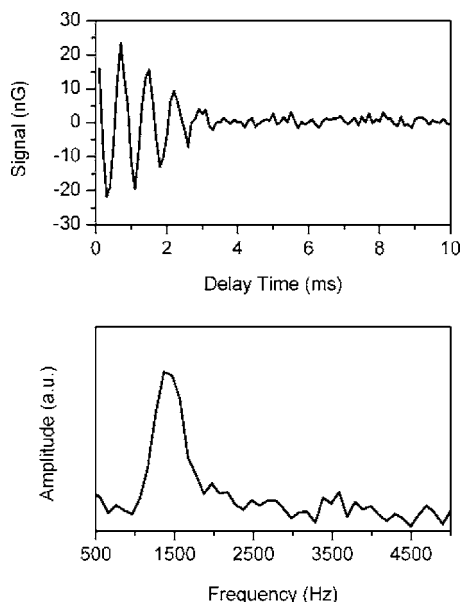
FIG. 11. Remotely measured point-by-point free induction decay and the corresponding Fourier transformation in frequency domain.

remotely, our pulse sequence differs from a regular CPMG pulse in that an additional $(\pi/2)_x$ pulse after the regular CPMG pulse is needed to encode the signal into longitudinal magnetization. The spin echo is therefore reconstructed by sweeping the delay time t between this encoding pulse and the last π_y pulse. The result (no signal averaging) is shown in Fig. 12, panels B and C. Panel B exhibits the data directly
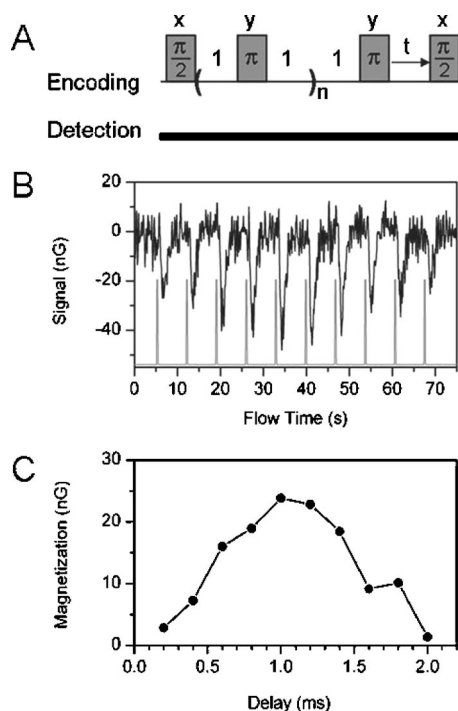

FIG. 12. The pulse sequence for the spin-echo reconstruction and the resulting spin echo. Panel A shows the pulse sequence. The echo time, which equals to the delay between two consecutive π pulses, is 2 ms, and the repetition number n is 50. The phases of the rf pulses are indicated above their respective positions. Panel B shows the data directly measured by the gradiometer, with the spikes indicating the timing of encoding. Panel C shows the base-line-corrected difference signal extracted from panel B.

measured by the gradiometer. The gray spikes indicate the start of the pulse sequences, each with a different t, which is swept from 0.2 to 2 ms, with 0.2 ms step size. Panel C shows the base-line-corrected difference signal extracted from panel B. The spin-echo signal is maximum at $t=1$ ms, as expected for the spin echo.

V. DISCUSSION AND OUTLOOK

The apparatus described here offers high sensitivity for detecting dc magnetic field produced by a magnetized sample. As demonstrated here (and in Ref. 21) it is well suited for low-field remote detection of NMR and MRI. In addition to the studies with water, we plan to perform NMR and MRI experiments using hyperpolarized xenon. The setup can also be used in non-NMR/MRI applications. For example, we have detected magnetic particles with a high sensitivity and a large carrier throughput (in our case, water; to be described in a separate publication). Additional applications in other fields, such as measuring the magnetic properties of nominally nonmagnetic ferroelectric materials and rock samples, are also in progress.

Further expected improvements include employing an array of rubidium cells as detectors and adopting a better geometric design. We plan to replace the external-cavity laser with an economic vertical-cavity surface-emitting laser, integrate the electronics, and employ fiber optics for laser-beam transmission. With these modifications, we expect to have an even less expensive and more convenient, potentially portable, apparatus for various practical applications.

[1] C. Cohen-Tannoudji, J. DuPont-Roc, S. Haroche, and F. Lalo, Phys. Rev. Lett. **22**, 758 (1969).
[2] N. R. Newbury, A. S. Barton, P. Bogorad, G. D. Cates, M. Gatzke, H. Mabuchi, and B. Saam, Phys. Rev. A **48**, 558 (1993).
[3] J. C. Allred, R. N. Lyman, T. W. Kornack, and M. V. Romalis, Phys. Rev. Lett. **89**, 130801 (2002).
[4] I. K. Kominis, T. W. Kornack, J. C. Allred, and M. V. Romalis, Nature (London) **422**, 596 (2003).
[5] D. Budker, V. Yashchuk, and M. Zolotorev, Phys. Rev. Lett. **81**, 5788 (1998).
[6] D. Budker, D. F. Kimball, S. M. Rochester, V. V. Yashchuk, and M. Zolotorev, Phys. Rev. A **62**, 043403 (2000).
[7] D. Budker, D. F. Kimball, V. V. Yashchuk, and M. Zolotorev, Phys. Rev. A **65**, 055403 (2002).
[8] M. V. Balabas, D. Budker, J. Kitching, P. D. D. Schwindt, and J. E. Stalnaker, J. Opt. Soc. Am. B **23**, 1001 (2000).
[9] W. Gawlik, L. Krzemien, S. Pustelny, D. Sangla, J. Zachorowski, M. Graf, A. O. Sushkov, and D. Budker, Appl. Phys. Lett. **88**, 13220 (2006).

[10] M. H. Levitt, *Spin Dynamics: Basics of Nuclear Magnetic Resonance* (Wiley, Chichester, 2001).

[11] P. T. Callaghan, *Principles of Nuclear Magnetic Resonance Microscopy* (Clarendon, New York, 1991).

[12] V. V. Yashchuk, J. Granwehr, D. F. Kimball, S. M. Rochester, A. H. Trabesinger, J. T. Urban, D. Budker, and A. Pines, Phys. Rev. Lett. **93**, 160801 (2004).

[13] I. M. Savukov and M. V. Romalis, Phys. Rev. Lett. **94**, 123001 (2005).

[14] R. McDemont, A. H. Trabesinger, M. Mück, E. L. Hahn, A. Pines, and J. Clarke, Science **295**, 2247 (2002).

[15] A. Wong-Foy, S. Saxena, A. J. Moulé, H.-M. L. Bitter, J. A. Seeley, R. McDermott, J. Clarke, and A. Pines, J. Magn. Reson. **157**, 235 (2002).

[16] S. K. Lee, M. Möβle, W. Myers, N. Kelso, A. H. Trabesinger, A. Pines, and J. Clarke, Magn. Reson. Med. **53**, 9 (2005).

[17] A. J. Moulé, M. M. Spence, S.-I. Han, J. A. Seeley, K. L. Pierce, S. Saxena, and A. Pines, Proc. Natl. Acad. Sci. U.S.A. **100**, 9122 (2003).

[18] J. A. Seeley, S.-I. Han, and A. Pines, J. Magn. Reson. **167**, 282 (2004).

[19] J. Granwehr, E. Harel, S. Han, S. Garcia, A. Pines, P. N. Sen, and Y. Q. Song, Phys. Rev. Lett. **95**, 075503 (2005).

[20] B. M. Goodson, J. Magn. Reson. **155**, 157 (2002).

[21] S. Xu, V. V. Yashchuk, M. H. Donaldson, S. M. Rochester, D. Budker, and A. Pines, Proc. Natl. Acad. Sci. U.S.A. (to be published).

[22] E. B. Alexandrov, M. V. Balabas, D. Budker, D. English, D. F. Kimball, C. H. Li, and V. V. Yashchuk, Phys. Rev. A **66**, 042903/1 (2002).

[23] V. V. Yashchuk, D. Budker, and J. R. Davis, Rev. Sci. Instrum. **71**, 341 (2000).

[24] K. L. Corwin, Z.-T. Lu, C. F. Hand, R. J. Epstain, and C. E. Wieman, Appl. Opt. **37**, 3295 (1998).

[25] D. Budker, D. J. Orlando, and V. V. Yashchuk, Am. J. Phys. **67**, 584 (1999).